



Slab effect of composite subassemblies under a column removal scenario



Wei Wang^{a,b}, Junjie Wang^{a,b}, Xin Sun^{a,b}, Yihai Bao^{c,*}

^a State Key Laboratory of Disaster Reduction in Civil Engineering, Tongji University, Shanghai 200092, China

^b Department of Structural Engineering, Tongji University, Shanghai 200092, China

^c Department of Civil and Environmental Engineering, University of California, Davis, CA 95616, USA

ARTICLE INFO

Article history:

Received 12 May 2016

Received in revised form 19 October 2016

Accepted 4 November 2016

Available online 13 November 2016

Keywords:

Beam-to-column subassembly

Experiment

Reinforced concrete slab

Progressive collapse

Detailed finite-element model

Arching action

ABSTRACT

This paper presents an experimental and computational study on the behavior of two composite subassemblies under a column removal scenario. The two specimens, designed as beam-joint-beam (B-J-B) subassemblies with reinforced concrete slabs on top of steel beams, were extracted from a prototype steel frame building with composite floor systems. One subassembly with the joint above the removed column was loaded under sagging deflection, and the other with the joint adjacent to the removed column was loaded under hogging deflection, simulating a center column removal scenario at a two-span beam-column subsystem. Detailed finite element models were also developed and analyzed for the two composite subassemblies. The observed failure modes were captured by the numerical models, and the computed load-versus-displacement curves agreed reasonably well with the measured data. To investigate slab effect, test results of the test specimens and steel subassemblies similar to the test specimens but without slab were compared. It showed that the load carrying capacities of the composite subassemblies were >63% higher than the steel subassemblies. Under sagging deflection loading, the composite subassembly showed a greater initial stiffness than the steel subassembly. Unlike the steel subassemblies, notable compressive axial forces were developed in beams of the composite subassembly subjected to sagging deflection at the early loading stages, indicating arching action contributed to the load resistance at small deformation as well as the initial stiffness. Contributions to the load capacity by resistant mechanisms, e.g. flexural action, arching action and catenary action were characterized and discussed.

© 2016 Elsevier Ltd. All rights reserved.

1. Introduction

In recent decades, great effort has been made in preventing progressive collapse which could cause a substantial casualty to building structures and human lives. Many abnormal loading conditions, such as fire, blast and vehicle impact may induce progressive collapse. The spread of an initial local failure from element to element, eventually resulting in the collapse of an entire structure or a disproportionately large part of it is commonly defined as progressive collapse [1]. The ASCE 7 Standard [1] recommends that resistance to progressive collapse be accomplished either implicitly, by providing minimum levels of strength, continuity, and ductility; or explicitly, by (1) providing sufficient strength to structural members that are critical to global stability or (2) providing alternate load paths so that local damage is absorbed and major collapse is averted through adequate connections and ties. When a major load-carrying member is damaged, an alternative load path is formed around failed structural members.

A series of testing programs have been conducted by the National Institute of Standards and Technology (NIST) to study the performance of moment-resistant frame assemblies under a column removal scenario

[2]. Liu [3] studied behavior of semi-rigid HSS beam-to-column connections through experimental and numerical analysis. Yang and Tan [4] carried out experimental tests on steel joints of simple and semi-rigid connections, such as web cleat, top and seat angle, flush end plate and extended end plate. Khandelwal and El-Tawil [5] investigated catenary action in moment resisting steel frames through computational simulations. Yang and Tan [6–8] studied the mechanical behaviors of bolted-angle beam-column joints under a column removal scenario. These studies show the dominant resistant mechanism of frame structures changes from flexural action at small deformation to catenary action at large deformation. For hollow section columns with non-flat surfaces (e.g. CHS), outer diaphragms are usually welded around the column. The adjacent open section (e.g. H-section) beams are connected to the column via the diaphragms using either bolted or welded connections (or a combination of the two approaches). Li and Wang [9] investigated the behavior of two types of outer-diaphragm connections under column removal scenario, with the welded-web and the bolted-web respectively. The test demonstrated the bolted-web connection is more redundant in strength and deformability. SHS/RHS column may hold the benefit of their flat surfaces, where a more straightforward connection detailing with internal diaphragms may be employed. Li and Wang [10] studied the effect of beam web bolt arrangement in H-beam to RHS column moment connection with internal diaphragms in resisting

* Corresponding author.

E-mail address: ybao@ucdavis.edu (Y. Bao).

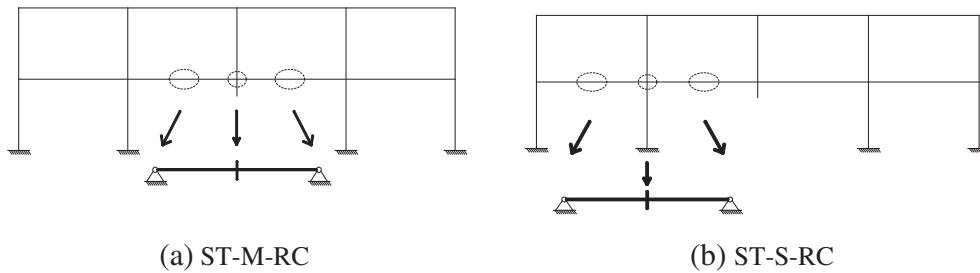


Fig. 1. Beam-joint-beam subassemblies.

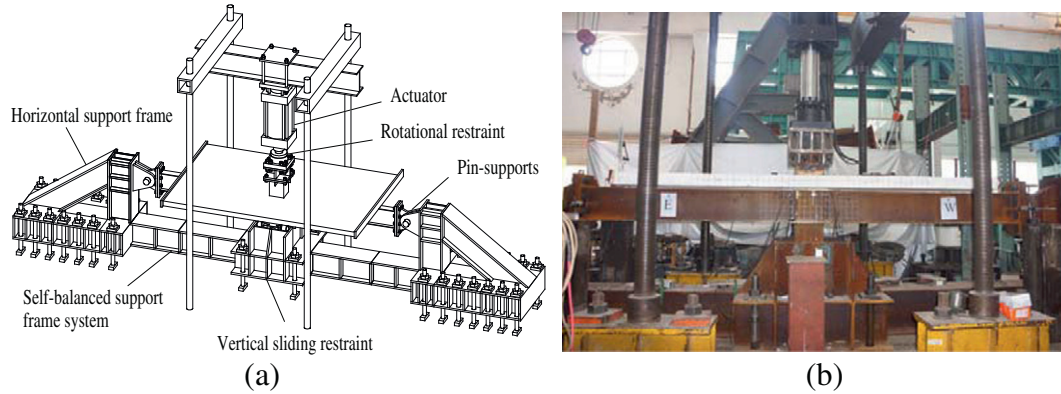


Fig. 2. Test setup.

progressive collapse. Results showed that arranging bolts in one row made the connection more robust than arranging bolts in two rows under column removal scenario. In order to achieve the convenience for fabrication, an alternative solution of internal diaphragms is to use short ‘through diaphragms’ (i.e. continuous plates ‘cutting’ through the column). In this case, the beam flange is directly welded to the edge of the diaphragm and the beam web can be bolted to the column with a normal shear tab connection. Qin and Wang [11] conducted experiments to investigate failure modes and load transfer mechanism in RHS column to H-beam connection with through diaphragms. The tensile force could be effectively retained after the beam flange failure, allowing the continuous development of catenary action.

Slab contribution to progressive collapse resistance has also been studied in recent years. Liew et al. [12] experimentally demonstrated rigid composite connections consisting of steel beams and reinforced concrete slabs developed a higher load-carrying capacity and better deformation ability than steel connections. Yasser Alashker et al. [13] used

finite element models to investigate the progressive collapse resistance of steel-concrete composite floor systems with single shear tab connections. Sadek et al. [14] explored the robustness of concrete deck-steel beam composite floor systems through computational simulations. Yu et al. [15] conducted numerical investigation on steel concrete composite frames including pin and rigid joints in preventing progressive collapse and showed that a rigid connection could improve the structural capacity to prevent progressive collapse. Demonceau and Jean-François [16] conducted experimental tests to simulate the loss of a column in a substructure which was extracted from a composite building with semi-rigid joints. Yang and Tan [17] conducted experimental tests to explore the behavior of semi-rigid composite beam-column joints with steel profile decking under a middle-column-removal scenario. Although resistance of progressive collapse has been considered as an important design requirement in published design guidelines, such as GSA [18] and DOD [19], the contribution of slab to progressive collapse resistance is not taken into account explicitly in practice due to lack of sufficient



(a) Horizontal support frame



(b) Vertical sliding restraint

Fig. 3. Horizontal support system and vertical restraint.

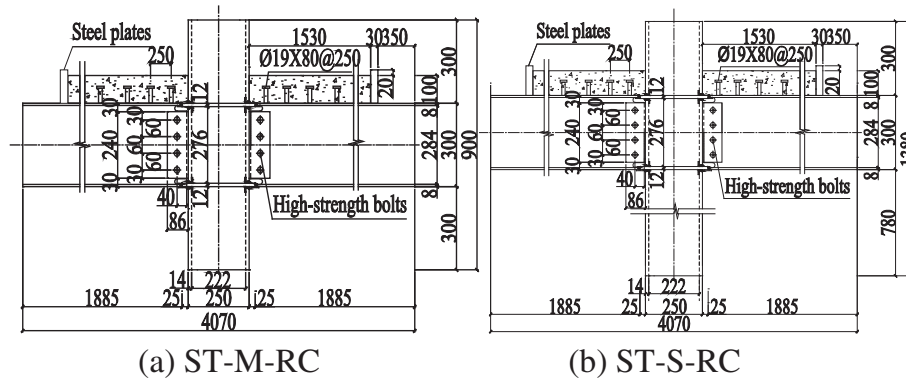


Fig. 4. Configuration of the subassemblies.

experimental data. In this paper, an experimental and numerical study on the slab effect of composite subassemblies with through diaphragm connection is presented. First, two composite subassemblies were tested under a center column removal scenario. Computational models were developed for the test specimens, and analysis results were compared with the experimental data. Next, the results from the composite subassemblies were compared with the results from the steel subassembly which were conducted in a former research [20] to demonstrate the slab effect on the load resistant capacity. Finally, the slab contribution to progressive collapse resistance was discussed in detail.

2. Test setup and specimens

2.1. Test setup

The test specimens were extracted from a prototype steel frame building with composite floor systems. As shown in Fig. 1, assuming that the inflection point is located at the middle of beam span, the internal force and deflection of a double-span beam-to-column subassembly are symmetric about the center column after its removal. Therefore, the double-span subassembly can be represented by a beam-joint-beam (B-J-B) subassembly comprised of two half-span beams with pinned supports at ends. It should be noted that the actual location of the inflection point is not exactly at the middle point of the beam span and also varies for composite or steel subassemblies. It is an approximate assumption that is made to facilitate the comparison of structural responses between the composite and steel subassemblies with same assumed conditions in the later part of this paper. Two types of composite subassemblies were tested as shown in Fig. 1 (a) and (b) respectively: one with the joint above the removed column and the other with the joint adjacent to the removed column. The name of specimens follows the nomenclature ST-M(S)-RC, where ST represents square tubular column, M represents middle joint and S represents side joint, RC represents reinforced concrete slab.

Fig. 2 shows the test setup. The specimens were pin-supported at two horizontal support frames and an additional horizontal restraint was provided by a self-balanced support frame system to simulate the restraint provided by surrounding structural components. A rotational restraint system was used to consider the rotational restraint to the center column from upper stories. With a sliding support at the bottom, the center column can only move in the vertical direction. Fig. 3 shows detailed configurations of the vertical restraint and the horizontal support frame. A displacement-controlled load was applied at the top of the center column. For Specimen ST-M-RC, the center column was pushed downward, while for Specimen ST-S-RC, the center column was pulled upward. The loading rate was <math>< 7\text{ mm/min}</math> with a 450 mm maximum loading range.

It should be mentioned that the more actual simulation of the side joint would be one cantilever beam, rather than two half-span beams as ST-S-RC. However, there were usually two identical side joints adjacent to the center column in practice, and in this case, it would be reasonable to regard the ST-S-RC as the sum of the two side joint.

2.2. Test specimens

Two composite subassemblies were designed as rigid connections with through diaphragms. Both specimens consisted of two composite beams connected to a center column with square hollow section. Complete penetration groove welds were used between the through diaphragm and beam flanges for the moment resisting connections. The detailed geometry and configuration of both specimens are described in Fig. 4. The cross-section view of the composite beam is shown in Fig. 5. The span of the beam is 4500 mm, which is equal to the distance between the inflection points. The cross sections of the steel column and beams are SHS250 \times 14 mm and H300 \times 150 \times 6 \times 8, respectively. The thickness of reinforced concrete slab is 100 mm, and the width is 700 mm. The slab was reinforced by two layers of 10 mm-diameter deformed bars along the longitudinal direction with 200 mm spacing and two layers of 6 mm-diameter deformed bars in the transverse direction with 200 mm spacing. One row of shear studs was welded along the beam length with 250 mm spacing to transfer shear forces between steel beams and the reinforced concrete slab, which achieved a partial shear connection. Two steel plates were placed at the ends of slab, and the longitudinal reinforcing bars were welded to the plates. The steel plates also served as a part of formwork during concrete casting. Photos of fabrication are shown in Fig. 6. The design of the specimens was based on the strong column-weak beam seismic design philosophy and specific requirements in Chinese codes [21]. The shear tabs have the same thickness as the beam web (6 mm) under the equal bearing capacity

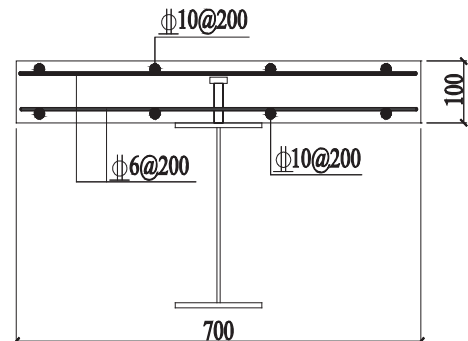


Fig. 5. Cross section view.

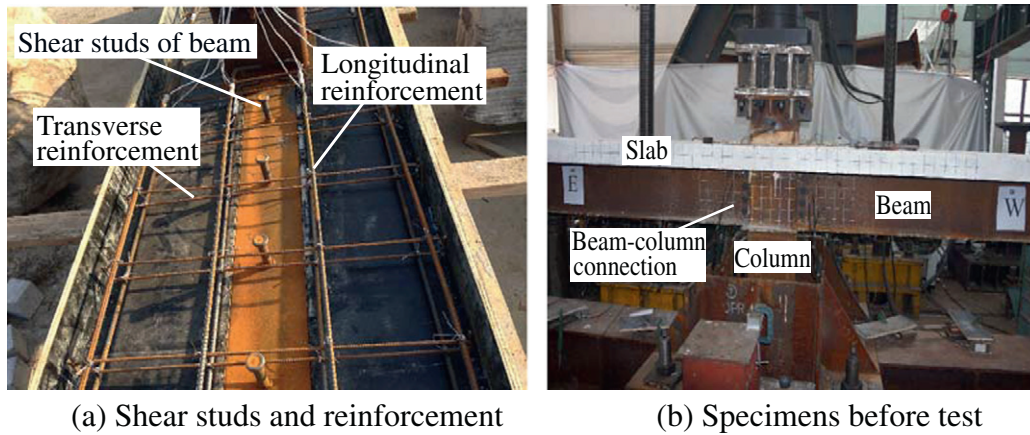


Fig. 6. Photos of specimen fabrication.

principle [22]. For each specimen, four M20 Grade-10.9 slip-critical high-strength bolts were used to connect the beam web and the shear tab.

3. Material properties

Table 1 gives the mechanical properties of the steel material, where f_y , and f_u are yield and tensile strengths respectively, and ϵ_f is the failure strain defined based on the ratio of initial cross sectional area to fracture cross sectional area. 150 mm \times 150 mm \times 150 mm concrete cubes were casted and cured under the similar condition as the slab. The concrete cube tests were performed in accordance with Chinese standard [23]. The average compressive strength of concrete cube is 37 MPa.

4. Instrumentation

The instrumentation plans of the two specimens are essentially the same. Sixteen line transducers were placed along the beam span to record the vertical deflections and the movements of the two pin-support rollers shown in Fig. 7(a).

Fig. 7(b), (c), (d) and (e) show the arrangement of strain gauges. A total of >80 strain gauges were placed in each specimen to measure strains at critical sections. The measured strains at Section W1 and E1 were used to calculate internal forces. The strain gauges attached to the most critical areas were to provide the strain conditions at Section W2/E2 and Section W3/E3. For the reinforced concrete slab, rebar strains were measured by embedded strain gauges at Section W2/E2, while concrete strains were measured by the strain gauges attached at the top/bottom surfaces of the slab.

5. Experimental results

5.1. Deflection and failure modes

The relationships of the vertical load versus the vertical displacement at the center column are shown in Fig. 8 for both specimens, where θ is the ratio of the vertical displacement at the center column to the length of half-span (2250 mm). The overall load-versus-displacement curve of Specimen ST-M-RC shows a similar trend seen in tests of reinforced concrete subassembly under center column removal [2], while the curve shape of Specimen ST-S-RC is more close to that observed in steel subassembly tests [20].

For Specimen ST-M-RC, an elastic behavior was observed before a vertical displacement of 36 mm at center column (A1, $\theta = 0.016$ rad). Rebar buckling was observed at the top layer reinforcing bars close to the center column. The bottom beam flange of Section W3 fractured

at a displacement of 93 mm (A2, $\theta = 0.041$ rad), leading to a sudden load drop from 294 kN to 118 kN. After that, the load bounced back to reach 236 kN. At a displacement of 167 mm (A3, $\theta = 0.074$ rad), the bottom beam flange of Section E3 fractured and the load was reduced to 125 kN. With the further increase of vertical displacement, the shear tab fractured followed by the beam web (A4, $\theta = 0.109$ rad; A5, $\theta = 0.147$ rad). The test was terminated when the actuator reached its maximum loading threshold at a vertical displacement of 420 mm ($\theta = 0.187$ rad). The photos of the specimen before and after test are shown in Fig. 9(a) and (b) respectively. The vertical deformation shapes during the loading process are plotted in Fig. 9(c) based on the measured deflection data along the beam span. The progression of failure is shown in Fig. 10.

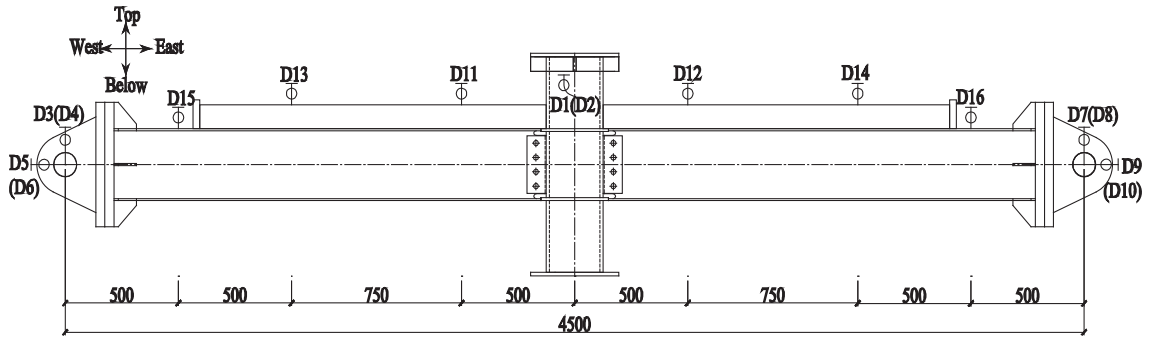
For Specimen ST-S-RC, the behavior of the specimen was elastic until the vertical displacement reached 42 mm (B1, $\theta = 0.019$ rad). The bottom beam flange of Section W3/E3 occurred local buckling at the displacement of 60 mm ($\theta = 0.027$ rad). At displacement of 176 mm (B2, $\theta = 0.078$ rad), the load suddenly dropped from 303 kN to 152 kN due to the fracture of the top beam flange at Section W3. After that, the load bounced back until the top beam flange at Section E3 fractured (B3), which led to another sudden drop of load from 276 kN to 170 kN. With the further increase of vertical displacement, the applied load increased gradually with several small drops due to the beam web fracture (B4, $\theta = 0.133$ rad) and the fracture of the upper layer reinforcing bars (B5, $\theta = 0.149$ rad; B6, $\theta = 0.160$ rad). The bottom beam flange at Section E3 fractured at a displacement of 400 mm (B7, $\theta = 0.178$ rad) with the applied load of 317 kN. The specimen lost vertical resistance completely after that. The photos of the specimen before and after test are shown in Fig. 11(a) and (b) respectively. The vertical deformation shapes during the loading process are plotted in Fig. 11(c) based on the measured deflection data along the beam span. Fig. 12 shows the development of failure.

Table 1
Material properties of steel and rebar.

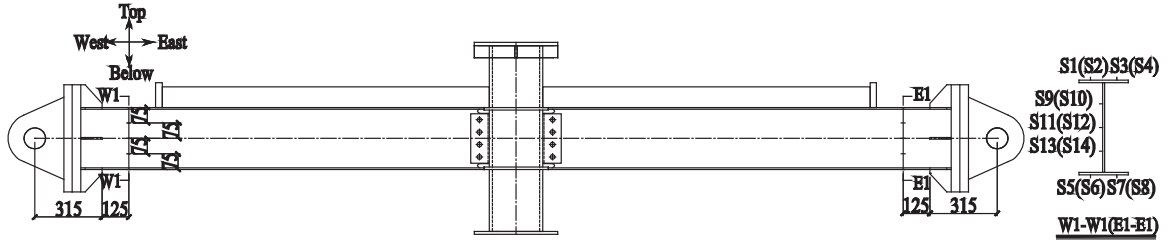
Components	f_y (MPa)	f_u (MPa)	ϵ_f
Straight section of RHS column ($t = 14$ mm) ^a	300	406	1.035649
Corner section of RHS column ($\phi = 14$ mm) ^a	468	545	0.96427
Beam flange ($t = 8$ mm) ^a	400	556	0.798581
Beam web ($t = 6$ mm) ^a	400	560	0.788584
Diaphragm ($t = 12$ mm) ^a	363	517	1.078891
Reinforcing bars $\phi 10^b$	528	713	0.755701
Reinforcing bars $\phi 6^b$	537	754	0.721505

^a Coupon tensile test.

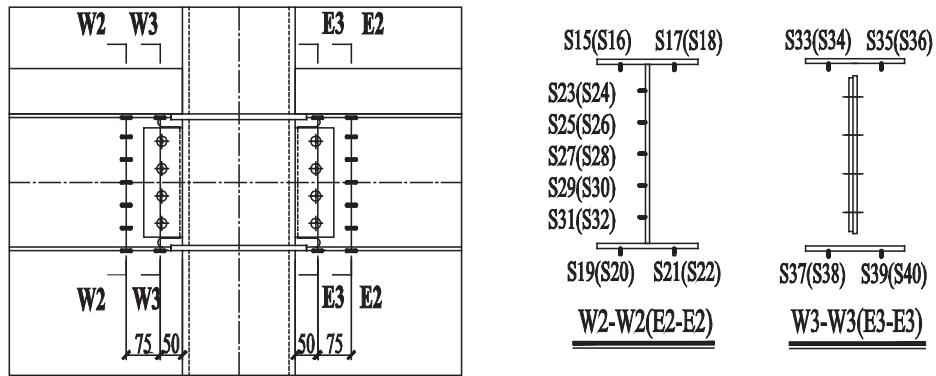
^b Rebar tensile test.



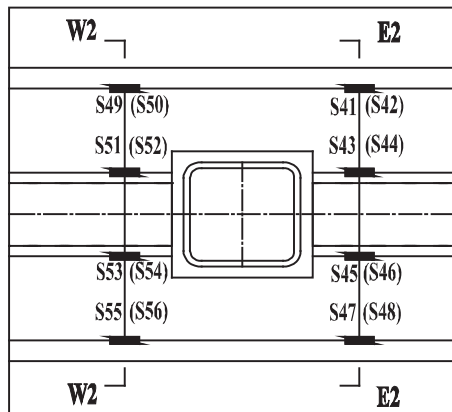
(a) Arrangement of line transducers



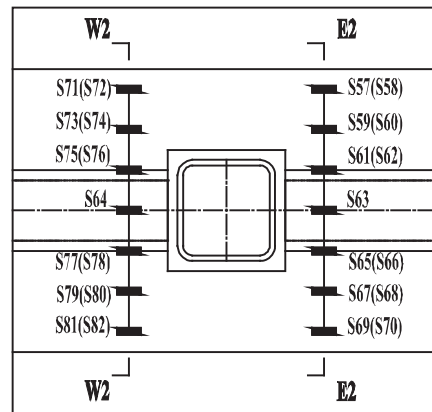
(b) Strain gauge arrangement at Section W1/E1



(c) Strain gauge arrangement at Section W2/E2 and Section W3/E3



(d) Strain gauge arrangement for slab rebar



(e) Strain gauge arrangement for slab concrete

Fig. 7. Arrangement of line transducers and strain gauges.

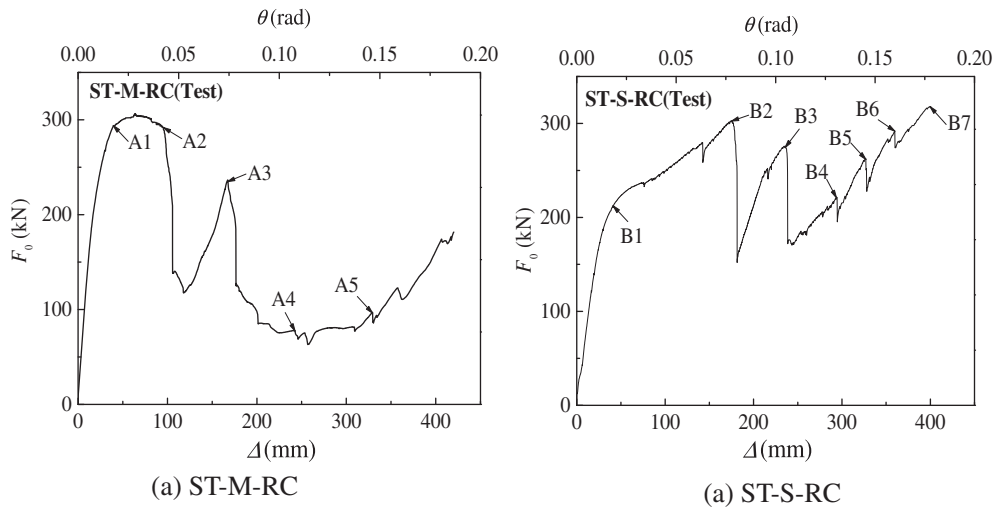


Fig. 8. Vertical load vs. displacement relationships of two specimens.

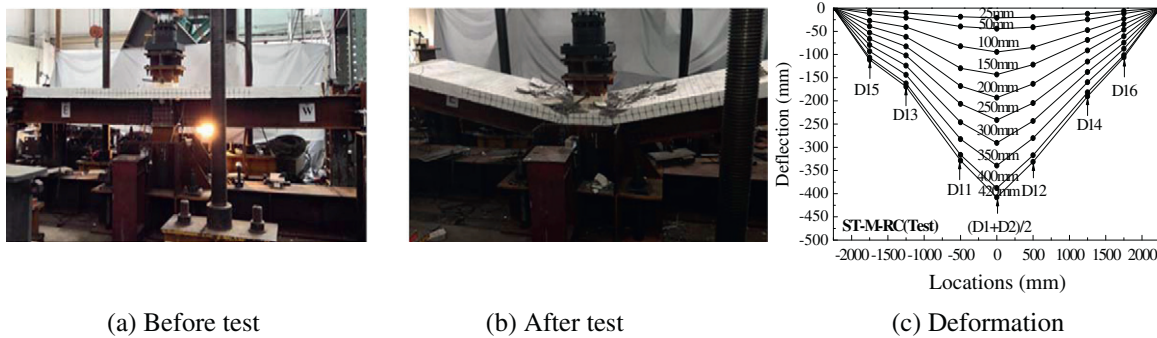


Fig. 9. Overall deformation of Specimen ST-M-RC.

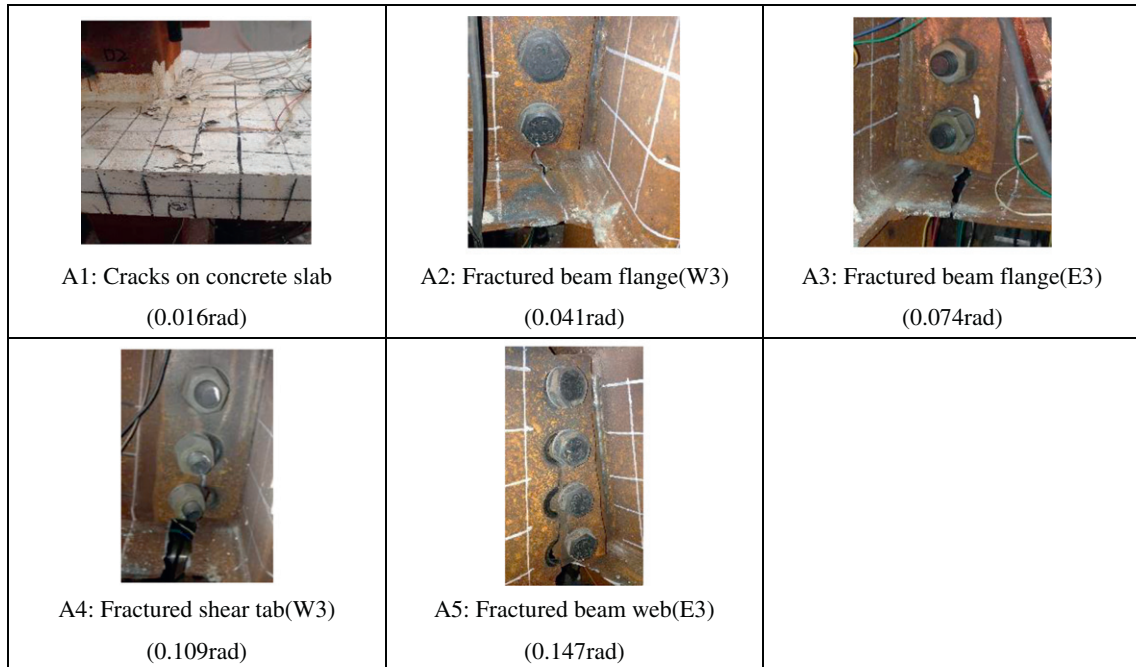


Fig. 10. Failure modes of Specimen ST-M-RC.

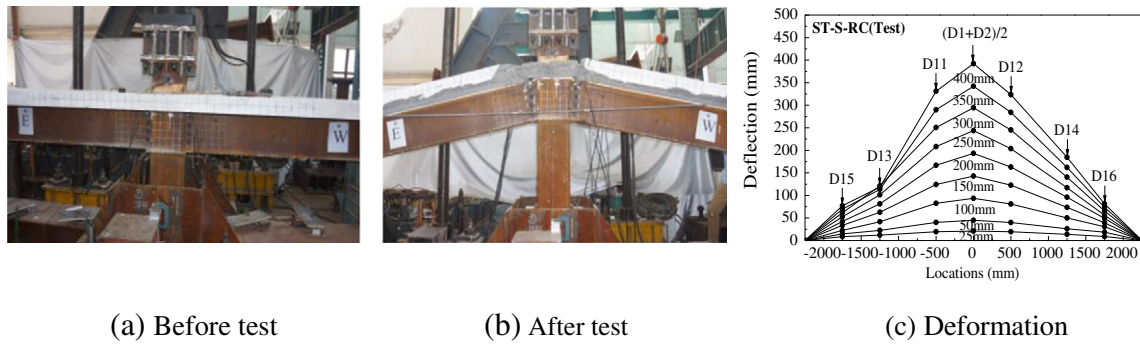


Fig. 11. Overall deformation of Specimen ST-S-RC.

5.2. Strain measurement

For Specimen ST-M-RC, measured strains at Section W1/E1 and Section W2/E2 are plotted in Fig. 13. Some strain gauges located at Section W2/E2 malfunctioned shortly after the test start as shown in Fig. 13(b) and (c). The strain development was in correspondence with the increase of vertical displacement of the center column. Fig. 13(a) shows that the neutral axis was located within the steel beam at the small deformation stages. With the development of deformation, strains at the top beam flange changed from compression to tension. At the late

stages, strains at Section W1/E1 were all in tension. As shown in Fig. 13(b) and (c), the concrete at the slab bottom surface and the bottom layer slab reinforcing bars were in tension at the small deformation stages, while the concrete at the slab top surface and the top layer slab reinforcing bars were in compression. It indicated that the neutral axis was located within the concrete slab. As described above, the strains of the slab top surface and steel upper flange were both compressive, and the strains of the slab bottom surface and steel lower flange were both tensile, which were caused by the partial shear connection between concrete slab and steel beam.

 <p>B1: Cracks on concrete slab (0.019rad)</p>	 <p>B2: Fractured beam flange(W3) (0.078rad)</p>	 <p>B3: Fractured beam flange(E3) (0.104rad)</p>
 <p>B4: Fractured beam web(E3) (0.133rad)</p>	 <p>B5: Ruptured rebar (0.149rad)</p>	 <p>B6: Ruptured rebar (0.160rad)</p>
 <p>B7: Fractured beam flange(E3) (0.178rad)</p>		

Fig. 12. Failure modes of Specimen ST-S-RC.

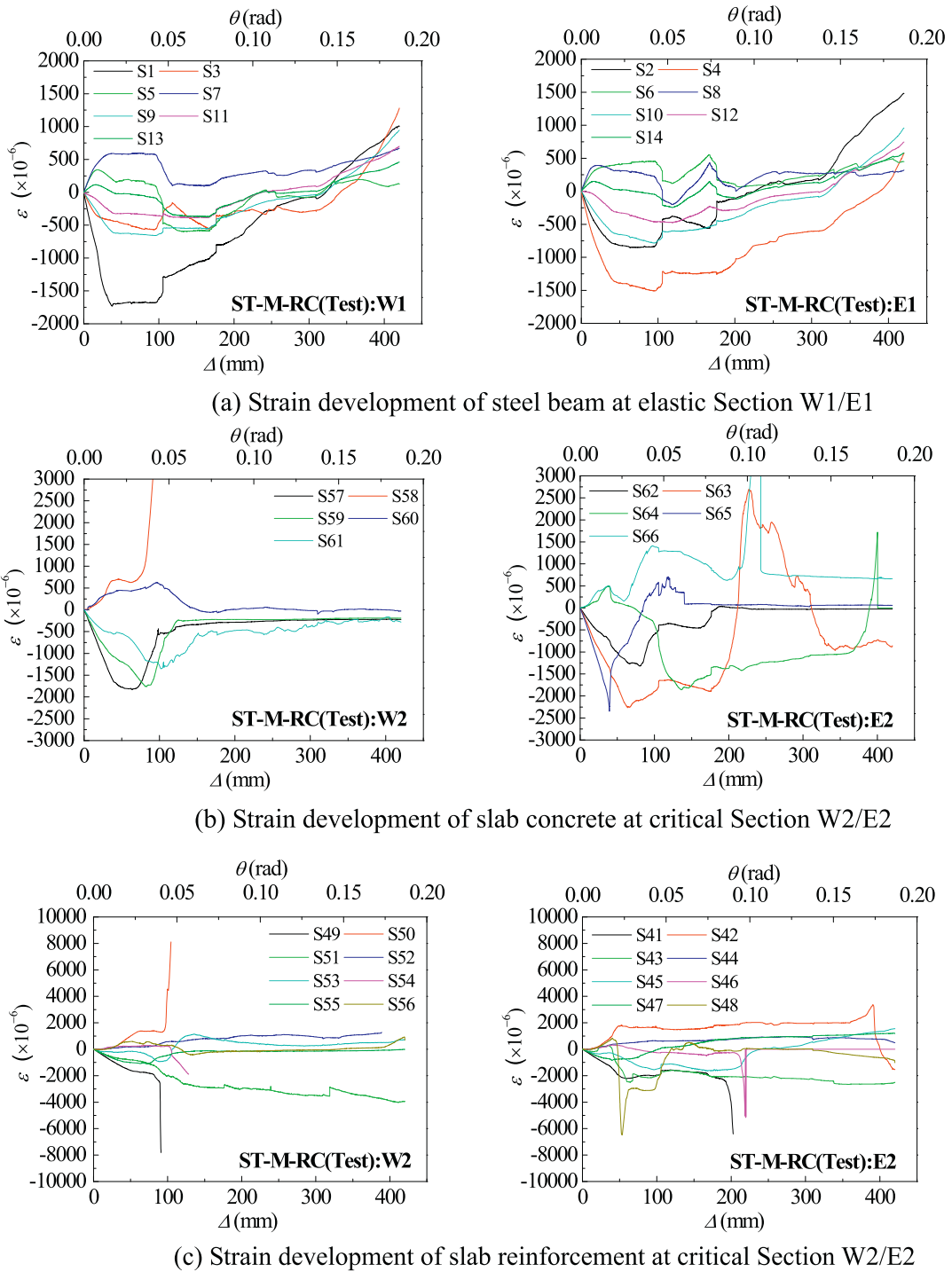


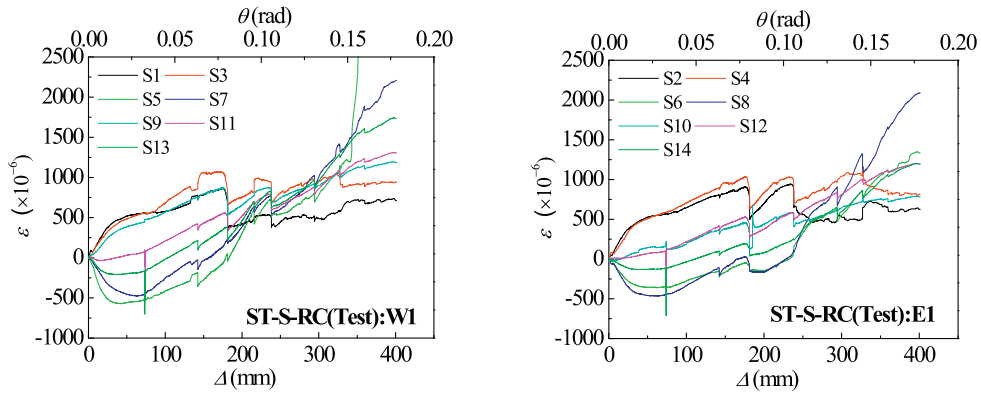
Fig. 13. Strain development of Specimen ST-M-RC.

For Specimen ST-S-RC, measured strains at Section W1/E1 and Section W2/E2 are plotted in Fig. 14. At the small deformation stages, strains at Section W1/E1 were almost symmetric about the section geometric center of the steel beam with the top beam flange in tension and the bottom beam flange in compression. Therefore, the neutral axis was close to the geometric central line of the beam section. With the development of displacement, strains at Section W1/E1 were all in tension. The obvious drops of strain were caused by the fracture of structural components. As shown in Fig. 14(b) and (c), the slab concrete and reinforcing bars were all in tension at the small deformation stages. The measured strains at Section W2/E2

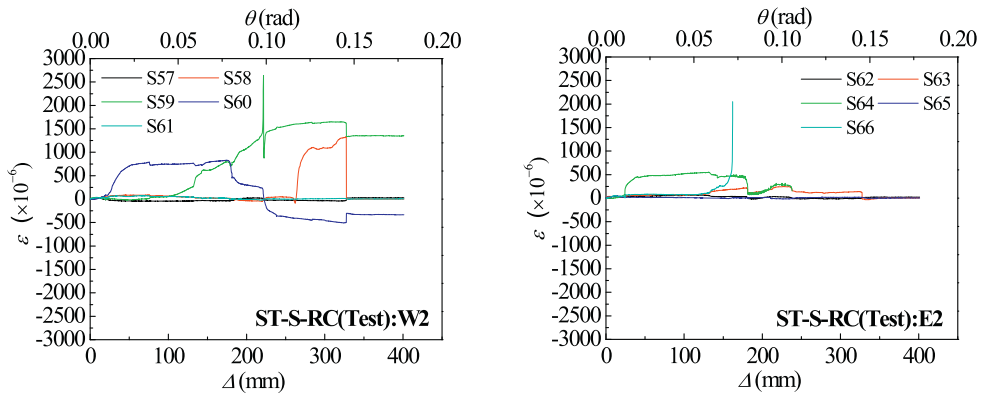
became unreliable at the large deformation stages due to failure of strain gauges.

6. Finite element simulation

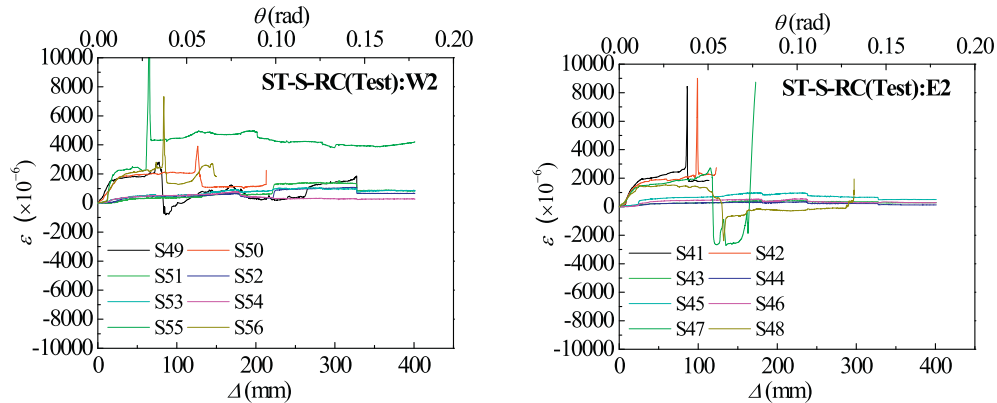
A general purpose finite element software ABAQUS was used to develop detailed models for the numerical study. The main objective of the numerical study is to verify and validate the modeling approach by comparing numerical results with experimental data. The numerical simulations were carried out using the explicit time integration approach with consideration of geometric and material



(a) Strain development of steel beam at elastic Section W1/E1



(b) Strain development of slab concrete at critical Section W2/E2



(c) Strain development of slab reinforcement at critical Section W2/E2

Fig. 14. Strain development of Specimen ST-S-RC.

nonlinearities, steel fracture, and concrete damage. The steel components except reinforcing bars and the slab concrete were represented by solid elements (C3D8R), while the reinforcement in the slab was represented by truss elements (T3D2). The stress-strain constitutive relationships of steel components were obtained from actual material coupon/bar tests. The modulus of elasticity (E) was 206GPa and Poisson's ratio (ν) was assumed to be 0.3. To simulate fracture of steel components, element erosion method was used. Once element strain exceeded the pre-specified fracture strain, individual element would be deleted in accordance with the "Damage for ductile metals" principle [24]. The fracture strain was calculated by the initial and fracture area of cross section in coupon test (shown in Eq. (1) and Table 1). The concrete damage plasticity model was

employed to simulate concrete behaviors. The compressive and tensile strengths of concrete material were obtained from concrete cube tests, and the stress-strain relationships were derived from the Chinese Code for Design of Concrete Structures [25] Appendix C (shown in Fig. 15). The modulus of elasticity (E) was approximate to be 30 GPa and Poisson's ratio (ν) was assumed to be 0.19. Damage parameters for compressive and tensile behaviors were defined to simulate the degradations of strength and stiffness after concrete damage.

$$\varepsilon_f = \ln\left(\frac{A_0}{A_{fracture}}\right) \quad (1)$$

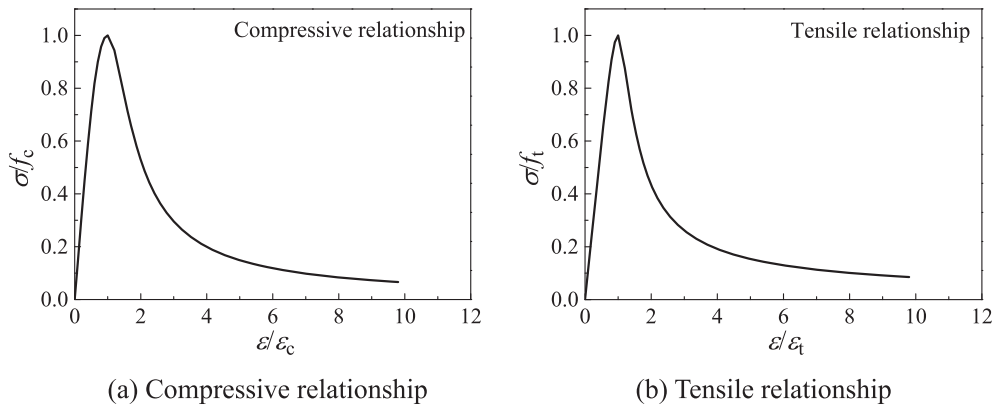


Fig. 15. Stress-strain relationship of concrete.

The bottom of studs was tied to the beam top flange. Interfaces between bolts and webs and shear plates were defined by contact with a friction coefficient of 0.4. The friction coefficient between steel beams and the concrete slab was assumed to be 0.2. The slab reinforcing bars and studs were embedded to concrete with the perfect-bond assumption. Mesh sizes of steel components and the slab concrete were 20 mm and 40 mm, respectively. Refined meshes with a size of approximately 2 mm were used in the connection zones where fracture may occur. The displacement-controlled load was applied at the top of the center column with a sufficiently slow rate to ensure that no dynamic effect was created. The top and bottom of the center column were restrained to slide only along the vertical direction (Z-direction). The finite element models, loading schemes and typical failure modes including flange fracture and shear tab fracture are shown in Fig. 16.

Fig. 17 shows the measured and computed applied load-versus-vertical displacement curves of Specimen ST-M-RC. The numerical result agreed well with the experimental result before fracture occurred at the beam bottom flanges. Unlike the experimental observation, the beam bottom flanges on both sides of the center column fractured simultaneously in the numerical simulation due to the idealized symmetry assumption, which led to a sudden drop of the applied load. The computed loads are higher than the measured loads at the large

deformation stages due to the limitations of the numerical model to accurately capture concrete damage behaviors. Fig. 18 shows the measured and computed applied load-versus-vertical displacement curves of Specimen ST-S-RC. The numerical result matched the experimental result reasonably well before fracture occurred at the beam top flanges. Unlike the experimental observation, the beam top flanges on both sides of the center column fractured simultaneously in the numerical simulation due to the idealized symmetry assumption, which led to a sudden drop of the applied load. For both cases, the fracture of flanges in the simulations occurred at a similar vertical displacement when the flanges at both sides of the column fractured in the tests. The accuracy of the simulation method is reasonably well at small deformation range ($\theta < 0.1$ rad), but, as the increase of displacement, the deviation of the concrete damage between simulation and actual response has led to a relative large discrepancy, especially for ST-M-RC.

7. Effect of slab

To investigate the slab effect, the test results of this study were compared to the test results from a previous study of a steel subassembly, which has similar configuration to the current specimens but without

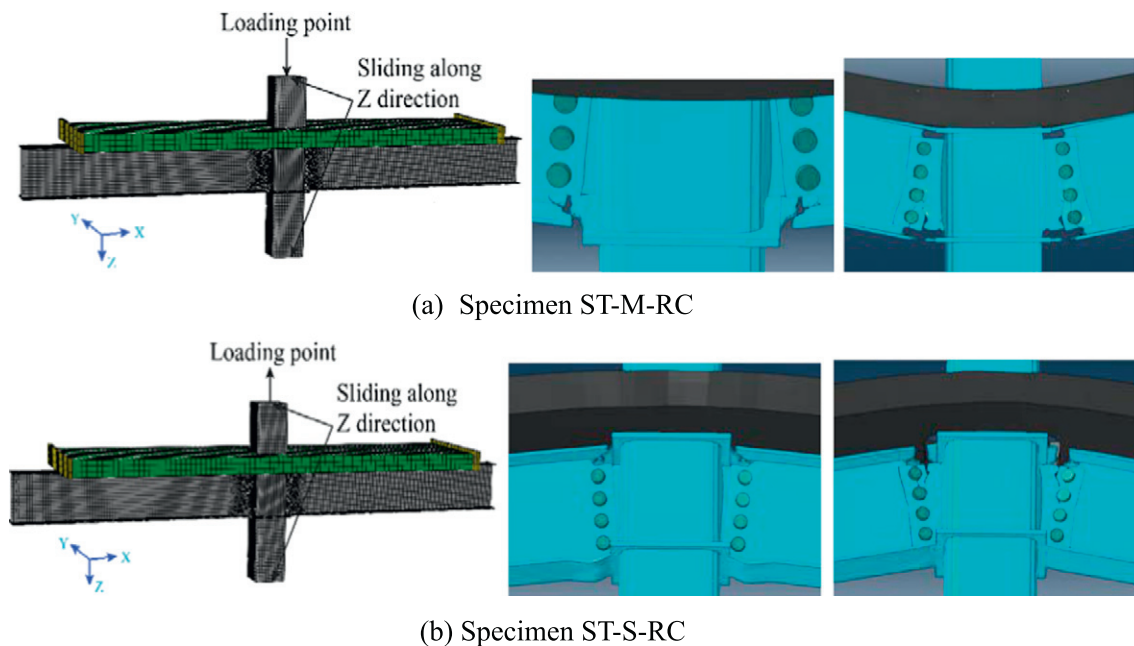


Fig. 16. FE modeling and typical failure modes.

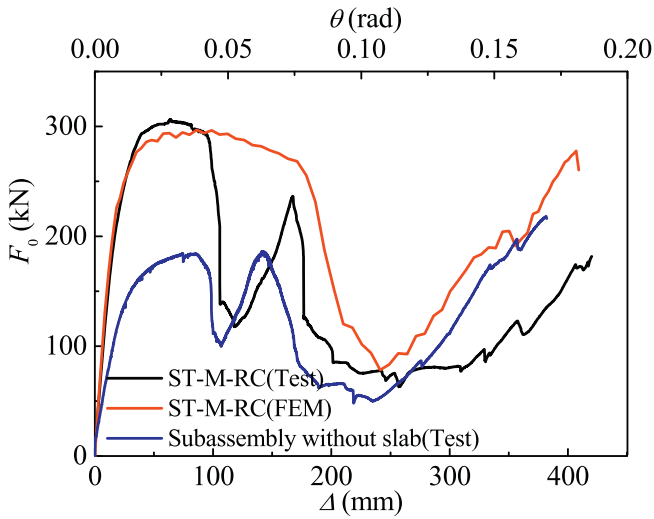


Fig. 17. Vertical load vs. displacement relationships of subassembly with middle joint.

slab. The referred steel subassembly was named as ST-WB in the paper by Wang et al. [20].

7.1. Structural response curve

The measured load–displacement curve of the steel subassembly under the same loading scheme as Specimen ST-M-RC is plotted in Fig. 17. As the result of composite action between the slab and steel beams, the load resistance and the initial stiffness of Specimen ST-M-RC are significantly higher than that of the steel subassembly. The measured maximum load of Specimen ST-M-RC is 307 kN (the corresponding displacement and chord rotation θ are 64 mm and 0.028 rad, respectively), a 65% higher than the maximum flexural load of 186 kN (141 mm, $\theta = 0.063$ rad) of the steel subassembly. The load–displacement curve of the steel subassembly under the same loading scheme as Specimen ST-S-RC is also plotted in Fig. 18. The measured maximum load of Specimen ST-S-RC is 303 kN (175 mm, $\theta = 0.078$ rad), a 63% increase compared to the maximum flexural load of 186 kN (141 mm, $\theta = 0.063$ rad) of the steel subassembly. No significant difference on the initial stiffness is seen between the composite and steel subassemblies since the contribution of concrete slab could be negligible under tension. As shown in Fig. 17 and Fig. 18, the shapes of the load–displacement curves of ST-M-RC and ST-S-RC are in significant difference. For Specimen ST-M-RC, the concrete slab was in compression under loading. A compressive arch was developed as the result of an offset between the neutral axes near the supports and near the center joint, respectively. No notable arching action was observed in Specimen ST-S-RC since the concrete slab cracked early under tension.

Fig. 17 also shows that the load-carrying capacity of the subassembly without slab (Test) developed faster than that of ST-M-RC (Test) in the catenary stage. This is because the compressive force developed in the concrete slab, which as shown in Fig. 19(a) counteracted and delayed the catenary action in ST-M-RC. In Fig. 19(a), the tensile axial force T was reduced by the compressive force C_c developed in the concrete slab as following:

$$T = T_s - C_c \tag{2}$$

where T_s is the tensile axial force in the steel beam nearby column. This reduction lasted until C_c diminished to a tiny level as the result of separation between the concrete slab and the steel column. As illustrated in Fig. 19(b), assuming the concrete slab was an intact rigid body and the steel beam was uniformly stretched between the center joint and the

supports, the rotation angle θ when the concrete slab departed from the steel column can be calculated as following:

$$L + d \cdot \tan\theta = \frac{L}{\cos\theta} \Rightarrow \theta = 7.48^\circ \tag{3}$$

where, L ($= 1530$ mm) is the length of the concrete slab determined as the distance between the steel column and the steel plates welded to the beam upper flanges, and d ($= 100$ mm) is the slab thickness. In general, L can be determined by the critical length that guarantees a full-shear connection between the concrete slab and steel beams. The corresponding vertical displacement at the center joint is 295 mm based on the calculated value of θ . It is noted that this displacement is close to the observed vertical displacement of 330 mm, where the axial forces at the composite beams started transiting from compression to tension (Fig. 20). As also indicated in Fig. 17, the catenary action was initiated at a similar vertical displacement of 320 mm. For the subassembly without slab, the catenary action was activated at a vertical displacement of 240 mm, significant earlier than the subassembly with slab (ST-M-RC). As discussed above, the delayed catenary action in ST-M-RC was mainly due to the compressive force developed in the concrete slab.

At the catenary stage, the computed result of ST-M-RC was close to the measured result of the subassembly without slab. It is mainly caused by the overestimated concrete damage in the material model, i.e. the compressive force in the concrete slab diminished much faster than it should be. In the test, although noticeable concrete damage was observed around the joint region, the considerable compressive force still could be developed through contact and bearing.

In this study, the slab edges parallel to the beams are free and slab membrane action is not considered since it will require a three-dimensional (3D) floor system test. It is expected that the existence of slab would further improve structural performance in the 3D system level where surrounding constraints are provided for slab to develop the membrane action other than the composite action.

7.2. Development of internal force

Based on the measured strains at Section W1/E1, the axial force N and bending moment M of Section W1/E1 can be calculated by following equations.

$$N = EA \sum_n \varepsilon \tag{4}$$

$$M = EI \frac{\Delta\varepsilon}{\Delta h} \tag{5}$$

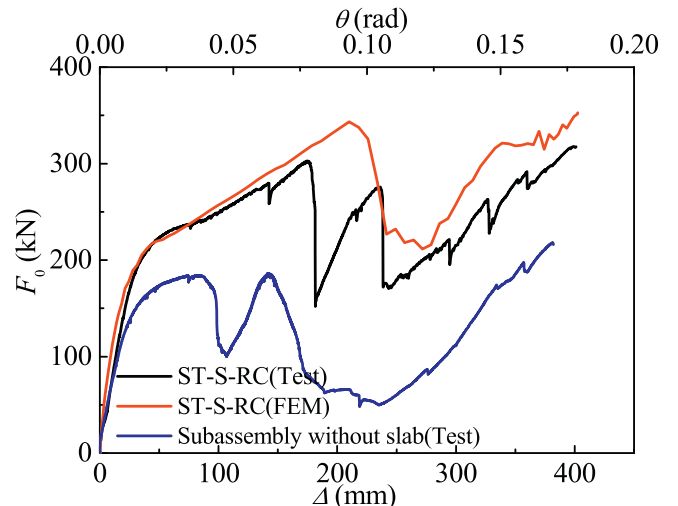


Fig. 18. Vertical load vs. displacement relationships of subassembly with side joint.

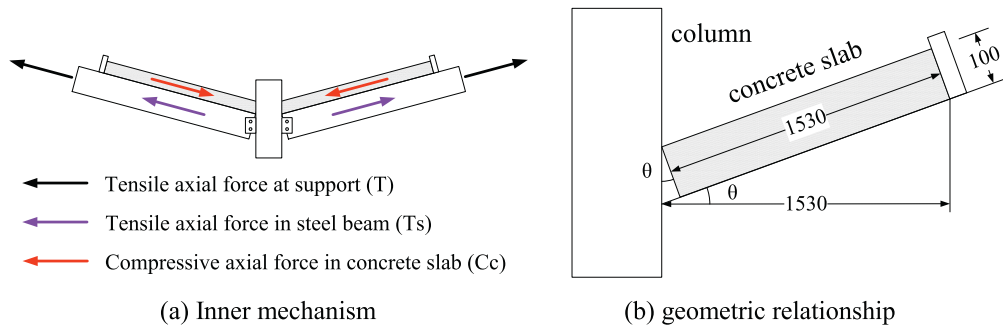


Fig. 19. The effect of concrete slab.

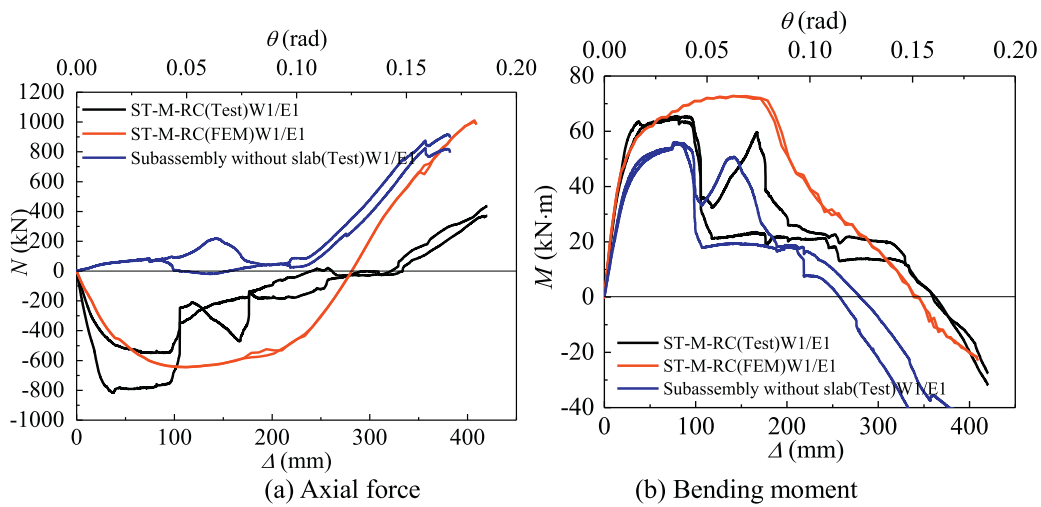


Fig. 20. Internal force development of subassembly with middle joint.

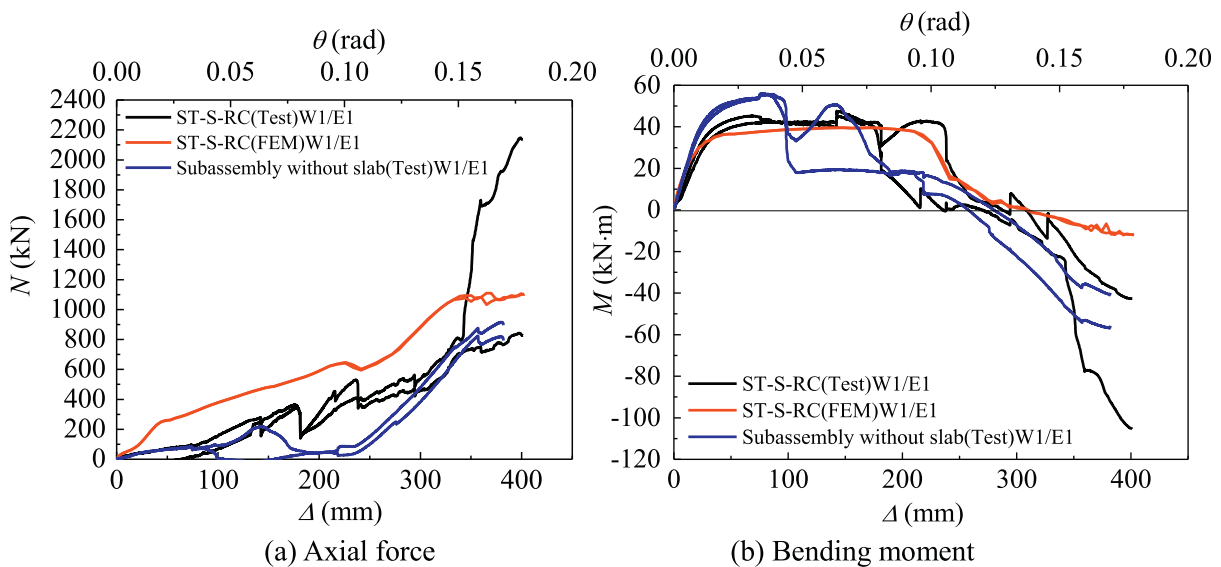


Fig. 21. Internal force development of subassembly with side joint.

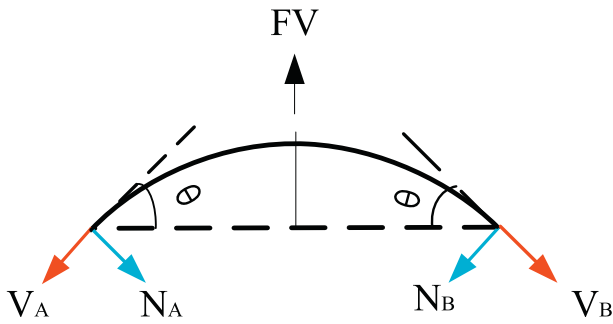


Fig. 22. Mechanical model of beam-to-column assembly.

where, E is the modulus of elasticity, A is the cross sectional area, $(\sum \varepsilon)/n$ is the average strain, I is the moment of inertia and $(\Delta\varepsilon/\Delta h)$ is the sectional curvature.

The developments of axial forces and bending moments at Section W1/E1 of Specimen ST-M-RC are plotted in Fig. 20 (a) and (b) respectively. Almost identical curves of the axial forces and bending moments are obtained for Section W1 and Section E1 based on the numerical simulation, while different curves of axial forces and bending moments at Section W1 and Section E1 are generated based on the measured strain data. It is because of the difficulty to keep a perfectly symmetric condition as assumed in the numerical simulation as in the real test due to the variation of material properties and the test apparatus. As shown in Fig. 20(a), compressive axial forces are developed in the beams of the composite subassembly at the initial loading stages. The axial forces change from compression to tension when the vertical displacement exceeds the beam depth, followed by changing sign of bending moments. Test results of the steel subassembly under the same loading scheme as Specimen ST-M-RC are also plotted in Fig. 20. No compressive axial forces is observed for the steel subassembly. It clearly indicates that compressive arching action is only developed in the composite subassembly as the result of slab effect, which increases the load resistant capability of the subassembly at flexural stage.

The development of axial forces and bending moments at Section W1/E1 of Specimen ST-S-RC are plotted in Fig. 21 (a) and (b) respectively. Same as the ST-M-RC subassembly, axial forces and bending moments of Specimen ST-S-RC obtained from the numerical simulation are almost identical at Section W1 and Section E1, while discrepancies are seen between the internal forces of Section W1 and Section E1 calculated based on the measured strain data. Unlike the ST-M-RC subassembly, the axial forces in the beams of Specimen ST-S-RC are in tension during the entire loading stages. The bending moment gradually changes sign from positive to negative after the beam top flange fractures. Test results of the steel subassembly under the same loading scheme as Specimen ST-S-RC are also plotted in Fig. 21. The composite and steel subassemblies exhibit a similar trend of internal force development, except higher forces are observed in the composite beams than in the steel beams.

7.3. Contributions to the vertical resistance by flexural, arch and catenary actions

For Specimen ST-S-RC, vertical load FV is carried by the beams connected to the removed column through axial forces and shear forces as shown in Fig. 22. The resistant force from catenary action (FA) is defined as the sum of the vertical components of the axial forces (V_A, V_B) and the resistant force from flexural action (FS) is defined as the sum of the vertical components of the shear forces (N_A, N_B). The contributions providing by two mechanisms are calculated by the following equations:

$$FA = V_A \sin\theta + V_B \sin\theta \tag{6}$$

$$FS = FV - FA \tag{7}$$

where, the axial forces (V_A, V_B) are calculated based on the measured strains at Section E1/W1.

The resistant forces FA and FS calculated based on the experimental data is plotted in Fig. 23. It shows that the flexural action almost contributed solely to the load resistance until yielding occurred. After that, the resistant force from catenary action mobilized and eventually exceeded FS , indicating the change of resistant mechanism from flexural action to catenary action. Fig. 24(a) and (b) shows the computed FS and FA of Specimen ST-S-RC and the steel subassembly without slab, respectively. The similar trend of the resistant forces is seen between the composite and steel subassemblies, indicating the existence of slab does not change the development of load resistant mechanisms.

For the Specimen ST-M-RC, the axial forces in the beams were compressive at the early loading stages (shown in Fig. 20). A compressive arch was formed as the result of the different locations of the neutral axes of Section W1/E1 and Section W2/W2. The resistance force (FV) was provided by flexural action and compressive arch action at small deformation and by catenary action at large deformation. Due to the compressive arch action, the calculating method of resistant forces of the composite subassembly (shown in Eq. (6) and (7)) is no longer applicable. Some researchers have proposed methods using the measured load to present the effect of compressive arch action in resisting progressive collapse [26,27]. If P_{cu} is the peak load under the compressive arch and flexural actions, and P_{yu} is the yield strength according to the conventional plastic analysis approach without considering the axial restraint of supports, the difference between P_{cu} and P_{yu} can be considered as the contribution of compressive arch action to the vertical resistant load. Based on the experimental results, P_{cu} is 306.6 kN and P_{yu} is 247 kN. Thus the vertical resistant force provided by compressive arch action is 59.6 kN or 19% of P_{cu} . Based on the numerical simulation, P_{cu} is 296.8 kN and P_{yu} is 248.6 kN. The contribution of compressive arch action to the vertical resistant load is 48.2 kN or 16% of P_{cu} .

7.4. Dynamic effect and evaluation of structural robustness

Due to the limitation of experimental conditions, the static testing method was adopted in the current study. However, under sudden column loss scenarios, it is important to consider the dynamic effect when

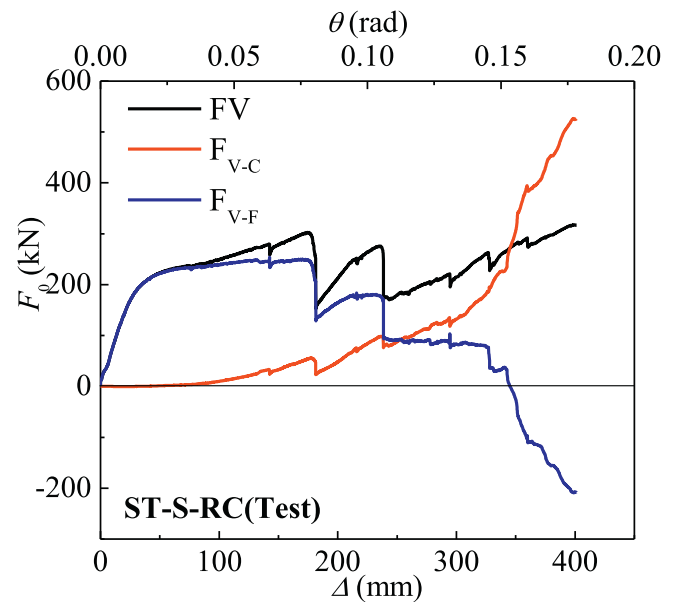


Fig. 23. Vertical resistance contributed by flexural mechanism (FS) and catenary mechanism (FA) of Specimen ST-S-RC in experimental test.

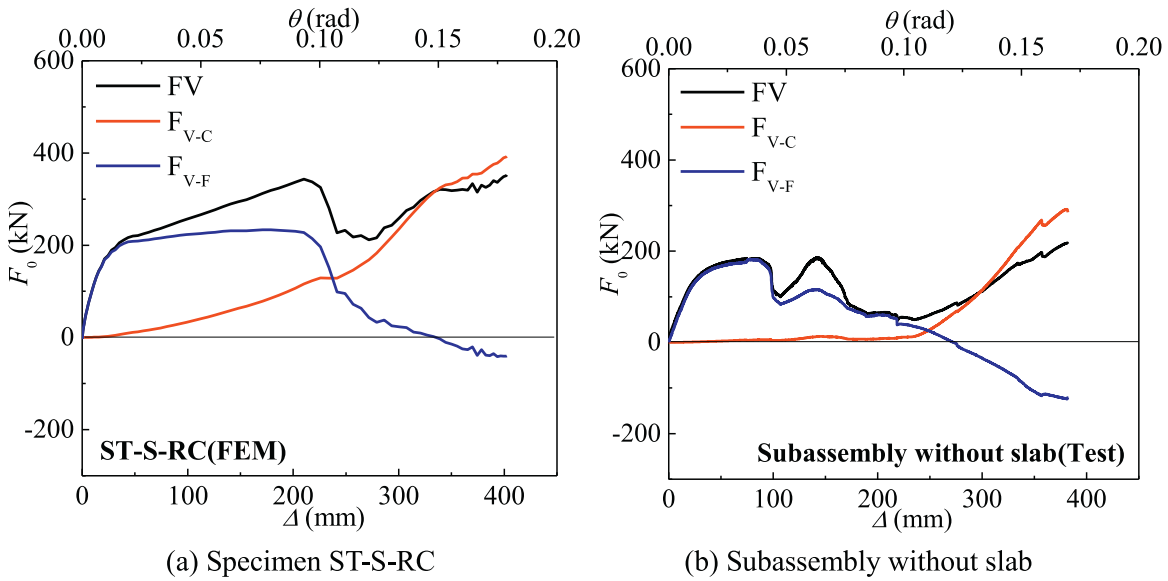


Fig. 24. Vertical resistance contributed by flexural mechanism (FS) and catenary mechanism (FA) of subassembly with side joint in FE modeling.

evaluating the robustness of building structures. Izzuddin et al. [28] proposed a simplified approach to evaluate the dynamic effect of building structures based on the nonlinear static response. As demonstrated in Fig. 25, for a given nonlinear static response, the maximum dynamic response associated with the sudden application of gravity load can be calculated based on the energy balance principle: the work done by the gravity load equals the stored internal energy.

In this study, the energy-based method was used to obtain the dynamic resistances of the steel and composite subassemblies under the sudden-column-removal scenario. As shown in Fig. 26, the maximum dynamic resistances of ST-M-RC and the steel subassembly occurred at the flexural stage, while the maximum dynamic resistances of ST-S-RC occurred at the catenary stage. Since the maximum dynamic resistance of ST-S-RC is only slightly higher than the peak dynamic resistance at the flexural stage, the peak dynamics resistance of ST-S-RC at the flexural stage was compared to that of ST-M-RC and the steel subassembly. Both composite subassemblies achieved much higher dynamic resistances (257 kN for ST-M-RC and 229kN for ST-S-RC) than the steel subassembly (149 kN), which is consistent with the static results. Comparing to ST-S-RC, the higher dynamic resistance of ST-M-RC is the result of the combined flexural and arching action.

The maximum dynamic resistance could be regarded as the capacity (C) of the subassemblies. The load demand (D) imposed on

the subassemblies can be calculated according to the corresponding tributary area. As long as C is greater than D, the subassembly could resist the sudden column loss without resulting in progressive collapse.

The plan view of the prototype building is shown in Fig. 27. The spans of girders and beams are l_{girder} (4.5 m) and l_{beam} (6 m), respectively. The floor system was designed for the dead load (DL) and live load (LL) of 5 kN/m² and 2 kN/m², respectively. According to the ASCE 7-10 (ASCE 2010) load combinations for extraordinary events, the capacity vs. demand ratio can be calculated as following:

$$\frac{C}{D} = \frac{\text{Capacity}}{\text{Demand}} = \frac{\text{Capacity}}{(1.2DL + 0.5LL)l_{girder} \cdot l_{beam}} \quad (8)$$

The capacity vs. demand ratios of ST-M-RC, ST-S-RC, and the steel subassembly are: 1.36, 1.21, and 0.79, respectively. It indicates that the

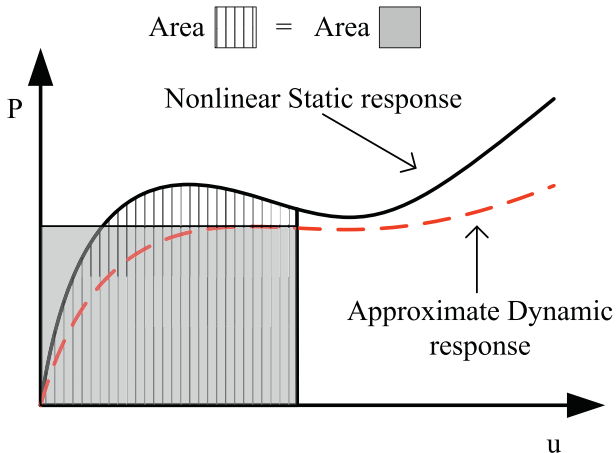


Fig. 25. Simplified dynamic assessment.

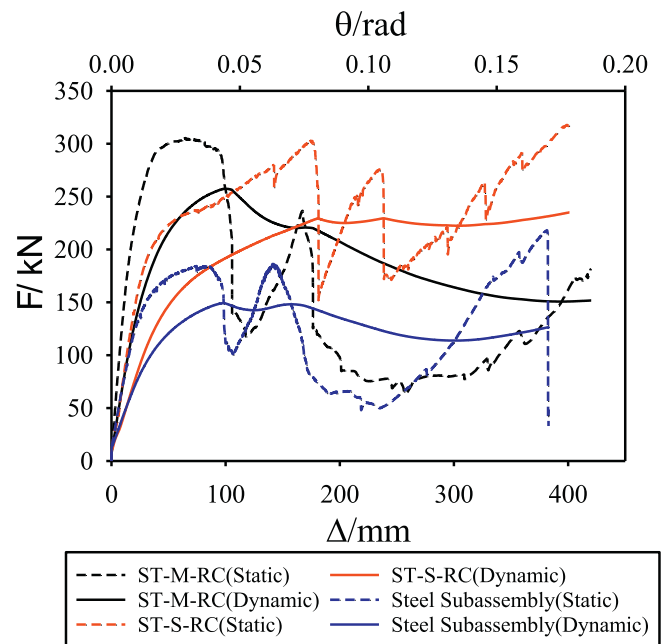


Fig. 26. Dynamic response of ST-M-RC and ST-S-RC.

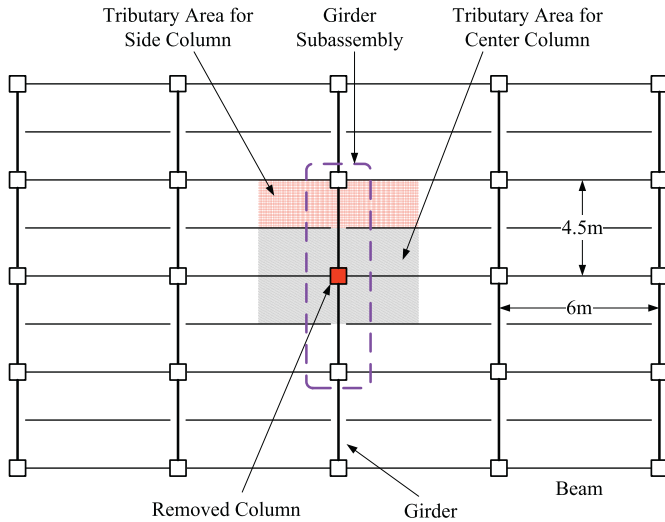


Fig. 27. The plan view of prototype building.

prototype building is able to withstand the sudden column loss when the slab is considered. The maximum beam span (7 m) can also be calculated by Eq. (8) when the capacity vs. demand ratio is 1.0.

8. Conclusion

Based on the experimental and numerical study, following conclusions are reached.

1. The developed detailed models captured the observed failure modes, and the computed applied load-versus-vertical displacement responses of two specimens agreed reasonably well with the measured data at flexural stage.
2. The experimental and numerical results showed that both composite subassemblies with slab carried at least 63% more load than the steel subassemblies without slab under the center column removal scenario. Under sagging deflection, the composite subassembly showed a greater initial stiffness than the corresponding steel subassembly.
3. Comparing the analysis results of Specimen ST-S-RC and the corresponding steel subassembly, the existence of slab did not change the development of resistant mechanisms: flexural action at small deformation and catenary action at large deformation. However, the compressive arching action was developed and contributed to the load resistance of Specimen ST-M-RC at the early loading stages as the result of slab effect. No notable compressive arching action was observed for the steel subassembly.

Acknowledgements

Financial support for this study was provided by the National “Twelfth Five-Year” Plan for Science & Technology Support Program through Grant No. 2015BAL03B01-2 and Shuguang Program through Grant No. 15SG19. Any opinions, findings, conclusions, or recommendations presented in

this paper are those of the authors and do not necessarily reflect the views of the sponsors.

References

- [1] American Society of Civil Engineers (ASCE), Minimum Design Loads for Buildings and Other Structures (SEI/ASCE 7–10), 2010 (Reston).
- [2] F. Sadek, J.A. Main, H.S. Lew, Y. Bao, Testing and analysis of steel and concrete beam-column assemblies under a column removal scenario, *J. Struct. Eng.* 137 (2011) 881–892 SPECIAL ISSUE: Commemorating 10 years of Research since 9/11.
- [3] Y. Liu, Behaviour of Beam-to-Tubular Column Connections under Extreme Loading Conditions, Imperial College London, London, 2012.
- [4] B. Yang, K.H. Tan, Experimental tests of different types of bolted steel beam-column joints under a central-column-removal scenario, *Eng. Struct.* 54 (2013) 112–130.
- [5] K. Khandelwal, S. El-Tawil, Collapse behavior of steel special moment resisting frame connections, *J. Struct. Eng.* ASCE 133(5), 2007, 646–655.
- [6] B. Yang, K.H. Tan, Robustness of bolted-angle connections against progressive collapse: Experimental test of beam-column joints and development of component-based models, *J. Struct. Eng.* ASCE 139 (9) (2012) 1498–1514.
- [7] B. Yang, K.H. Tan, Experimental test of different types of bolted steel beam-column joints under a central-column-removal scenario, *Eng. Struct.*, 54, 2013, 112–130.
- [8] B. Yang, K.H. Tan, Numerical analyses of steel beam-column joints subjected to catenary action, *J. Constr. Steel Res.* 70 (2011) 1–11.
- [9] L. Li, W. Wang, Y. Chen, Y. Lu, Experimental investigation of beam-to-tubular column moment connections under column removal scenario, *J. Constr. Steel Res.* 88 (2013) 244–255.
- [10] L. Li, W. Wang, Y. Chen, Y. Lu, Effect of beam web bolt arrangement on catenary behavior of moment connections, *J. Constr. Steel Res.* 104 (2015) 22–36.
- [11] X. Qin, W. Wang, Y. Chen, Y. Bao, Experimental study of through diaphragm connection types under a column removal scenario, *J. Constr. Steel Res.* 112 (2015) 293–304.
- [12] J.Y. Richard Liew, T.H. Teo, N.E. Shanmugam, C.H. Yu, Testing of steel-concrete composite connections and appraisal of results, *J. Constr. Steel Res.* 56 (2) (2000) 117–150.
- [13] Y. Alashker, S. El-Tawil, F. Sadek, Progressive collapse resistance of steel-concrete composite floors, *J. Struct. Eng.* 136 (10) (2010) 1187–1196.
- [14] F. Sadek, S. El-Tawil, H.S. Lew, Robustness of composite floor system with shear connections: modeling, simulation, and evaluation, *J. Struct. Eng.* 134 (11) (2008) 1717–1725.
- [15] M. Yu, X. Zha, J. Ye, The influence of joints and composite floor slabs on effective tying of steel structures in preventing progressive collapse, *J. Constr. Steel Res.* 66 (2010) 442–451.
- [16] J.F. Demonceau, J.P. Jaspart, Experimental test simulating a column loss in a composite frame, *Adv. Steel Constr.* 6 (3) (2010) 891–913.
- [17] B. Yang, K.H. Tan, Behaviour of composite beam-column joints under a middle-column-removal scenario: experimental tests, *J. Struct. Eng.* 140 (2) (2014).
- [18] General Service Administration (GSA), Progressive Collapse Analysis and Design Guidelines for new Federal Office Buildings and Major Modernization Projects, 2003 (Washington, D.C.).
- [19] Department of Defense (DOD), Design of buildings to resist progressive collapse, Unified Facilities Criteria (UFC) 4-023-03, 2009 Washington, D.C.
- [20] W. Wang, F. Cheng, Q. Xi, C. Yiyi, L. Ling, Performance of practical beam-to-SHS column connections against progressive collapse, *Eng. Struct.* 106 (2016) 332–347.
- [21] Ministry of Construction of China, Code for Design of Steel Structures (50017-2003), 2003 (Beijing).
- [22] Y. Kurobane, J.A. Packer, J. Wardenier, N. Yeomans, Design Guide for Structural Hollow Section Column Connections, (CIDECT), 2004.
- [23] Ministry of Construction of China, Standard for test method of mechanical properties on ordinary concrete (50081-2002), 2002 (Beijing).
- [24] ABAQUS Analysis User's Manual Version 6.7. ABAQUS Inc.; 2007.
- [25] Ministry of Construction of China, Code for Design of Concrete Structures (50010-2010), 2010 (Beijing).
- [26] K. Qian, B. Li, J.X. Ma, Load-carrying mechanism to resist progressive collapse of RC buildings [J], *J. Struct. Eng.* 141 (2) (2015) 04014107.
- [27] Y. Su, Y. Tian, X. Song, Progressive collapse resistance of axially-restrained frame beams [J], *ACI Struct. J.* 106 (5) (2009) 600.
- [28] B.A. Izzuddin, A.G. Vlassis, A.Y. Elghazouli, D.A. Nethercot, Progressive collapse of multi-storey buildings due to sudden column loss—part I: simplified assessment framework, *Eng. Struct.* 30 (5) (2008) 1308–1318.